7 8

9

On the omnidirectionality of a system with eight spinning rods for wake control of a circular cylinder in laminar regime

I. A. Carvalho^{a,*}, G. R. S. Assi^b

^aDepartment of Mechanical Engineering, EPUSP, University of São Paulo, SP, 05508-030, Brazil ^bDepartment of Naval Arch. & Ocean Engineering, EPUSP, University of São Paulo, SP, 05508-030, Brazil

Abstract

We investigate the omnidirectionality of a system comprised of a main circular cylinder (of diameter D) fitted with eight rotating rods (of diameter d = D/20) acting as wake-control devices over the incoming flow of velocity U_{∞} and viscosity ν . The gap between rods and main body is G/D1/100. Finite-volume simulations were conducted at a Reynolds number $Re = U_{\infty}D/\nu = 100$ in two configurations: One in which all rods spun with the same angular velocity (case 0); and another, in which the rotation speeds were inspired by potential-flow theory (case 1). We show through analysis of hydrodynamic coefficients, vorticity contours and power consumption that both configurations reduced mean drag, eliminated the vortex wake, and were negligibly affected in terms of power loss by the angle of attack. Nevertheless, the two cases showed different behaviours regarding omnidirectionality: While case 1 became ever "more omnidirectional" (that is, less susceptible to the angle of attack to render null mean lift and suppress vortex shedding) with increasing angular speeds, case 0 produced an imbalanced, yet steady, wake that led to larger absolute values of mean lift at higher speeds. The relative importance of each rod of the system is explained, and it becomes clear that merely introducing actuating power into the rods' motion does not translate directly into better wake control. Rather, it is essential that the rotation speeds are appropriately weighted according to the position of the rods relative to regions of boundary and shear layer, and wake of the main body.

Keywords: Omnidirectionality, vortex-shedding suppression, wake control, drag reduction, bluff bodies.

Preprint submitted to Journal of Fluids and Structures

October 20, 2023



^{*}Corresponding author: amorim.icaro@usp.br (I. A. Carvalho)

1. Introduction

Bluff bodies have been observed to produce and be subjected to different wakes and motions according to the flow past them. Since its earliest observation over a century ago (Von Kármán, 1954), the typical Kármán-Bénard vortex street has inspired many studies and applications in a multitude of fields. Once the boundary layer separates from the body, it becomes free shear layers influenced by the instabilities of the flow in the near-wake region. These structures carrying high levels of vorticity roll up and subsequently give rise to the alternating vortex shedding mechanism (Gerrard, 1966). Consequently, the structure is acted upon by cyclic loads (that may lead to fatigue and failure) with an intensity that depends on the dimension of the body (D), the viscosity of the fluid (ν) and the velocity of the incoming flow (U_{∞}) , all colapsed into a single non-dimensional, the Reynolds number $Re = U_{\infty}D/\nu$. As it has been observed, due to transversal and longitudinal components of the resulting load (relative to the direction of the flow, termed lift and drag, respectively) fluid-structure interaction occurs, represented by low-frequency vortex-induced motion (VIM) typical of large structures (Fujarra et al., 2012), and vortex-induced vibrations (VIV), both rooted, in most practical applications, in the vortex-shedding phenomenon (Blevins, 1990; Williamson and Govardhan, 2004), although recent results show that VIV also occurs prior to vortex-shedding in very low Reynolds numbers (Dolci and Carmo, 2019).

Several forms of passive and active actuators have been devised to control vortex shedding according to the need of power input (Zdravkovich, 1981). Whereas in the context of bluff body flows, passive methods are characterised by surface protrusions (e.g., helical strakes, shrouds, fairings and splitter plates, Baek and Karniadakis, 2009; Assi et al., 2009; Korkischko and Meneghini, 2011); active methods (Choi et al., 2008) rely on the power input to spin shrouds (Mittal, 2001), deliberately vibrate the body (Blackburn and Henderson, 1999; Du and Sun, 2015), blow or suction the flow (Bearman, 1967; Chen et al., 2013). Although different mechanisms have been implemented, they generally attempt to enhance flow control through interaction with the boundary or shear layers, or with the developed wake (Modi et al., 1990).

One promising approach is that of inserting shrouds around a main body. Strykowski and Sreenivasan (1990) observed that a single (passive) control rod of diameter d significantly smaller than D was able to entirely suppress vortex shedding for appropriate Reynolds numbers. This limitation was observed by Mittal and Raghuvanshi (2001) and others, who further advanced the

subject by employing a spinning rod instead of a passive one. This idea stems from the scope of the Moving Surface Boundary-layer Control (MSBC) technique, originally for aerofoils (Modi et al., 1990) to delay stall. For bluff bodies, MSBC implementation aims to use a secondary body to inject momentum into the boundary layer of the larger body and thus move the separation points further downstream (Cicolin et al., 2021). Amongst the benefits, MSBC (i) delays separation, (ii) weakens vortex interaction within the thinner wake and (iii) reduces hydrodynamic loads.

A plethora of (numerical and experimental) studies followed those of Strykowski and Sreenivasan (1990), some of them devoted to sensitivity analysis of the near-flow to the insertion of a secondary passive body (Marquet et al., 2008) to establish the concepts of sensitivity to base-flow modifications and to a steady force; that were later employed in the study of a set of active bodies by Patino et al. (2017). These authors found that an optimised distribution of control rods may reduce drag. Mittal (2001) and others explored different passive arrangements of spinning rods, varying the proportionality of the rods d/D, the gap G/D between the main body and the rods, the number of rods, their relative positions, etc. (Korkischko and Meneghini, 2012; Silva-Ortega and Assi, 2017a, to cite a few). Recently, the same system was studied in the context of finite cylinders, where end effects were present (Carvalho and Assi, 2023b,a). A particular setup of interest to the present work is that of Silva-Ortega et al. (2015) with 8 rods, see figure 1. This study of the passive wake-suppression mechanism showed that this configuration stood out amongst others with two, four and eight rods with respect to lift attenuation. Despite a drag increase, this setup showed later to be able to mitigate the peak amplitude of VIV when compared with the case of a plain cylinder and when compared to other configurations (Silva-Ortega and Assi, 2017a). Contrarily, the other configurations investigated by Silva-Ortega and Assi (2017a) were less effective in the suppression of hydrodynamic loads and response amplitude, and rendered the system more prone to galloping, VIV, or both, cumulatively.

The same setup of 8 rods was later undertaken in the context of an active mechanism (MSBC). Silva-Ortega and Assi (2017b) conducted experiments that presented a reduction in the amplitude of drag and lift in the arrangement portrayed by figure 1; more importantly, they showed that MSBC was able to reduce sustained vibrations (as those of the baseline case). The authors pointed out, however, that changes in the angle of attack α (i.e. the orientation of the incoming flow in relation to the device) could affect the performance of the entire system in controlling the

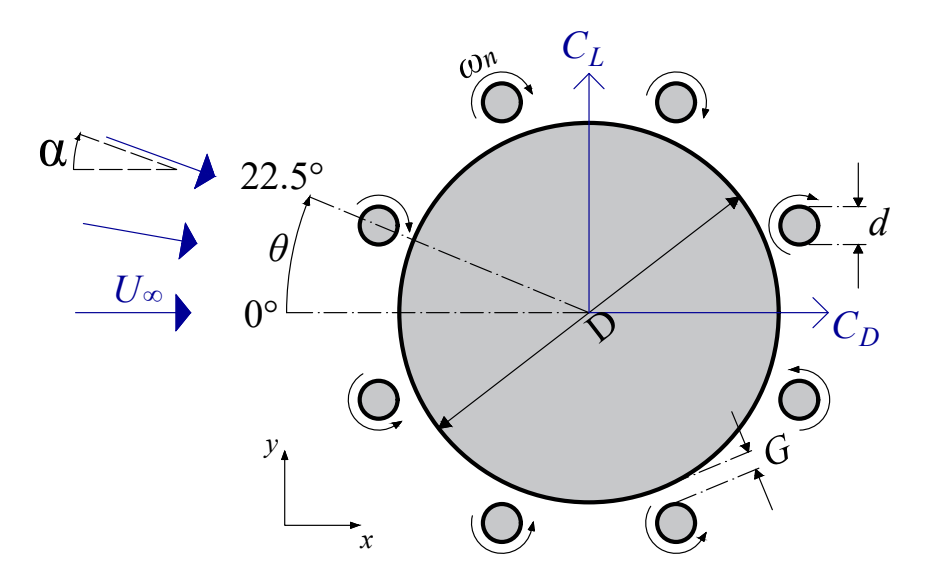


Figure 1: Incoming flow U_{∞} at different angles of attack α past a system comprised by a main cylinder (of diameter D) and rotating control rods (of diameter d). The gap between the rods and the main body is G. Drag and lift are denoted C_D and C_L , respectively. Rods are placed at positions conventioned by θ . In the active mechanism, angular velocities are $\omega_n \neq 0$.

hydrodynamic loads.

Advancing on flow topology, incipient numerical simulations of this system evaluated vortex shedding in laminar and turbulent regimes and revealed that the rods effectively eliminated the vortices of the former and subsided in the latter (Assi et al., 2018, 2019). The difference in behaviour was due to the *Re*-regime and its inherent vortex dynamics features. Later, Carvalho and Assi (2022), based on a potential-flow-inspired setup of rotations (Carvalho et al., 2021), corroborated that indeed the arrangement of 8 rods could eliminate the vortex wake, given sufficient rotation speed to the rods; and, beyond that, exposed that a more efficient system resulted from spinning some rods faster than others. In fact, the authors also remarked that the rods had a similar effect to that of "laminarising" the flow, as the (turbulent viscosity of the) eddies progressively disappeared.

These past studies have advanced in the comprehension of the impact of the system of 8 rods on the flow dynamics, hydrodynamic loads and more particularly, on the interaction of the fitted rods with the shear layers. Nevertheless, we note that neither these experiments nor these numerical simulations have tackled the effect of the angle of attack. This was remarked by Silva-Ortega and Assi (2017b). Indeed, to the best of our knowledge, previous works were generally concerned with a fixed angle of attack or, when the body was yawed, a suppressing system was not employed (Vakil

and Green, 2009), except for the work of Wu et al. (2016). In the latter, the authors evaluated an asymmetric passive system with auxiliary lines that was able to suppress vortex shedding at all evaluated angles of attack, but depending on this parameter, the time-averaged streamlines presented the formation of bubbles, related to non-null hydrodynamic forces.

Our study aims to fill this void in the literature for Re = 100, varying the angle of attack and the rotation speeds in cases in which the rods spin with the same speed and in which their rotations follow a potential-flow analogy. We further uphold considerations of actuating power required to counteract shear and mean drag in this active mechanism.

1.1. Objective

In the present work, we investigate how a system comprised of a main larger body of diameter D fitted with eight slender rods of diameter d/D = 1/20 is influenced by the angle of attack α of the incoming flow U_{∞} ranging from 0° to 22.5°. The rotating rods are equally spaced at angular positions θ , at intervals of 45° around the main body, offset by 22.5° from the frontal stagnation point, as presented in figure 1. The gap G/D = 1/100 is measured between the walls of the cylinders. Our analysis considers the hydrodynamic loads, wake topology and power spent to rotate the rods. Furthermore, we inspect the individual roles of the rods within the system in terms of lift, C_L , and drag, C_D . Two cases are considered:

- Case 0: rods spin with the same velocity ω_0 (note that upper and lower rods spin in opposite directions)
- Case 1: rods spin with different velocities ω_n , based on the theoretical potential-flow field around a circular cylinder.

2. Method

The incompressible, unsteady flow of a Newtonian fluid is governed by the Navier-Stokes and continuity equations,

$$\rho\left(\frac{\partial U_i}{\partial t} + U_j \frac{\partial U_i}{\partial x_j}\right) = -\frac{\partial p}{\partial x_i} + \mu \frac{\partial^2 U_i}{\partial x_j \partial x_j},\tag{1}$$

$$\frac{\partial U_j}{\partial x_j} = 0. (2)$$

which were solved by a finite-volume method in the C++ open-source OpenFOAM library. Each term followed an appropriate discretisation scheme to mitigate truncation and discretisation errors; and inspired by the physics of the problem, whether the discretised term corresponded to a diffusive or a convective term. Only second-order schemes were employed to mitigate truncation errors.

The transient term $\partial U_i/\partial t$ on the left-hand side of equation 1 was discretised according to an implicit backward scheme. The divergence term $U_j\partial U_i/\partial x_j$, representative of the convective flow, was discretised with a linear upwind scheme. Gradients were computed using a least squares method, which entailed the gradient of the pressure term and the Laplacian term on the right-hand side of the same equation (computed as the divergence of the gradient). A non-orthogonality correction was required for the calculation of the Laplacian term whenever the surface of the cells and the line connecting the centres of two adjacent cells were not perpendicular to one another (skewness effect). Because our numerical scheme was cell-centred, interpolation of values to the surface of the cells was carried out with linear interpolation. Surface normal gradients were determined in the same way as the Laplacian terms.

Equations 1 and 2 were solved at each time step using the aforementioned discretisation scheme and the following boundary conditions: for the incoming flow, far away from the system, the velocity U_{∞} and fully developed pressure gradient $\nabla p = 0$ were specified. A no-slip boundary condition was prescribed on the walls of the bodies, either by imposing the tangential velocity of the rotating rod or by zeroing the velocity in the case of the main body and passive rods. The outflow was given by null pressure and null null directional derivative of the velocity in the outward flow direction.

A schematic drawing of the geometry and of the directions mentioned above employed in the simulations is shown in figure 2, where the rods were not represented for ease of visualisation. The O-grid topology was selected to enable the variation of the angle of attack α of the incoming flow, and it is fully represented in figure 3, where the meshing of different regions are exhibited for clarity. The distance from the centre of the main body to the outmost circumference enclosing the entire grid was given by 32D. Refinement was emphasised near the walls of the bodies with small cells, and the grid expansion ratio was modest, of 1.1 outward of the rods into the near-field of the entire system and also between the rod and the main body, and 1.029 outward of the entire system into the far-field domain. In the circumferential direction between rods the grid refinement ratio was given by 0.99 to sufficiently capture the wake and yet provide an economical solution.

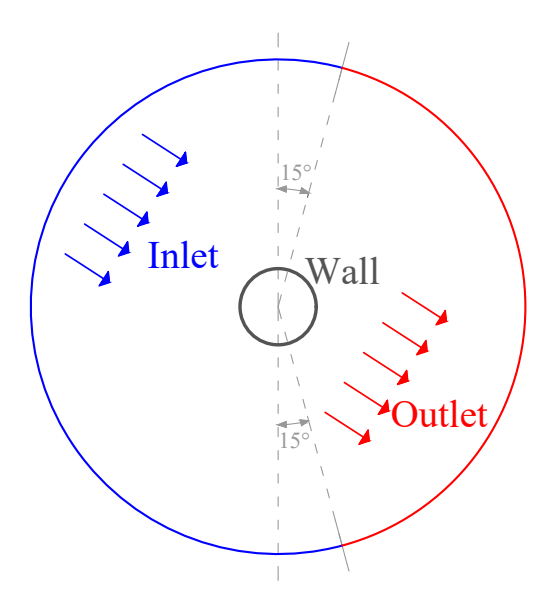


Figure 2: Inlet (blue), outlet (red) and wall (grey) boundary conditions assigned to the O-grid geometry. Only the main body is represented. For the rods, the same condition was applied, however, there the wall rotated with angular velocity ω_n . The figure is not to scale for clarity.

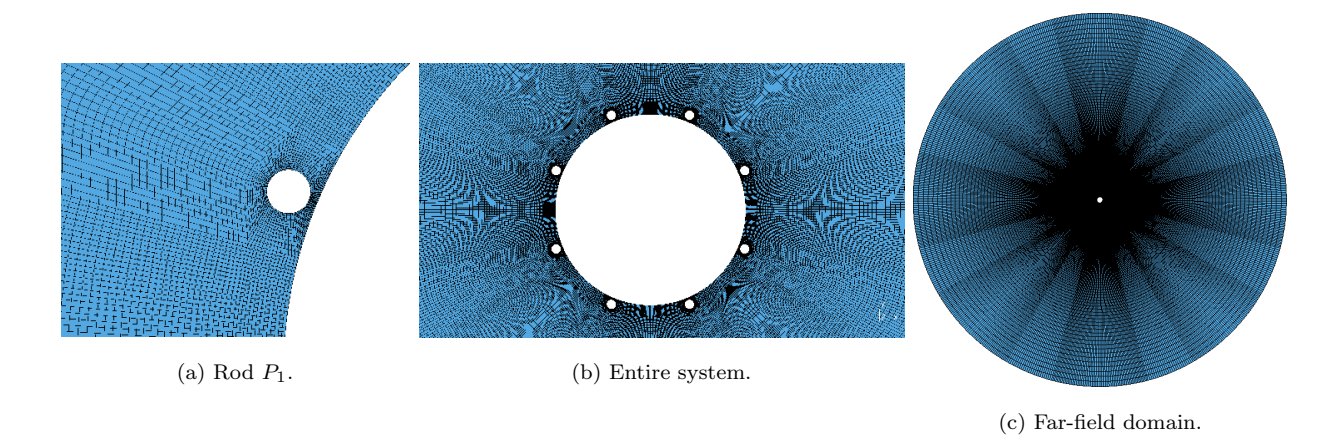


Figure 3: Different regions of the structured grid.

A pertinent issue in resolving equations 1 and 2 in incompressible flow is that the pressure p and the velocity U_i are neither related by an equation of state, nor there is a transport equation for p. To couple pressure and velocity, the SIMPLE algorithm (Patankar, 1980) iterated the numerical solution at each time step to ensure that the momentum and continuity equations were concurrently satisfied by the resolved field. Tolerances of 10^{-4} and 10^{-8} were respected, respectively, for the determination of the pressure and for the velocity at each time step, looped through for at least 10 iterations. Relaxation factors were not applied. Rhie and Chow's interpolation was used to prevent the checker-board effect.

Provided with the resolved field, pressure and viscous effects were considered over the surface of each body to compute hydrodynamic forces, conveniently decomposed into drag F_D and lift F_L components that were non-dimensionalised into force coefficients $C_D = F_D/(0.5\rho U_\infty^2 D)$ and $C_L = F_L/(0.5\rho U_\infty^2 D)$, respectively, based on the aforementioned quantities and fluid density ρ .

2.1. Definition of rotation rates and time step

Input rotation speeds for the control rods were inspired by the commonplace problem of the potential flow around a bare cylinder. At the radial distance r = D/2 + G + d from the centre of the body, the velocities V_n were determined from the potential-flow field about a plain cylinder at angular coordinates θ :

$$V_n = U_\infty \left\{ \hat{r} \left[\cos \left(\theta \right) \right] \left[1 - \frac{(D/2)^2}{(D/2 + G + d)^2} \right] + \hat{\theta} \left[-\sin \left(\theta \right) \right] \left[1 + \frac{(D/2)^2}{(D/2 + G + d)^2} \right] \right\} \cdot \hat{\theta}, \quad (3)$$

where θ is the position of the rods when the system was considered at different angles of attack:

$$\theta = \theta_n - \alpha \tag{4}$$

$$\theta_n = \pm 22.5^{\circ} \pm 45^{\circ} (n-1) - \alpha, \quad n = 1, \dots, 4$$
 (5)

where θ_n marks the position of the rods for $\alpha = 0$ (see figure 1). In equation 5, the positive sign is for the upper rods and the negative is for the lower rods. In case 0, α ranged from 0° to 20.0°, while in case 1 the upper limit was of 22.5°, in steps of 2.5°. For each θ , the corresponding velocities were obtained from potential flow.

These linear velocities were assigned to each rod in the problem involving the main body and equipped rods following the same procedure performed by (Carvalho and Assi, 2023a, but then only for $\alpha = 0$). That is, rods' velocities were given by $\omega_n = \zeta V_n/(d/2)$ for the upper rods and

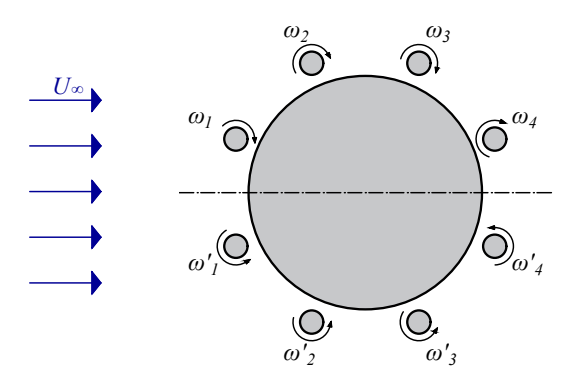


Figure 4: Angular velocities of the upper rods of the system were defined in case 1 as $\omega_n = \zeta V_n/(d/2)$, where V_n are the velocities attained in potential flow about a bare cylinder at polar coordinates r = D/2 + G + d, and $\theta = \theta_n = 22.5^{\circ} + 45^{\circ}(n-1)$. $\zeta > 0$ is a free variable. For the lower rods, $\omega'_n = -\omega_n$. The figure is not to scale for clarity.

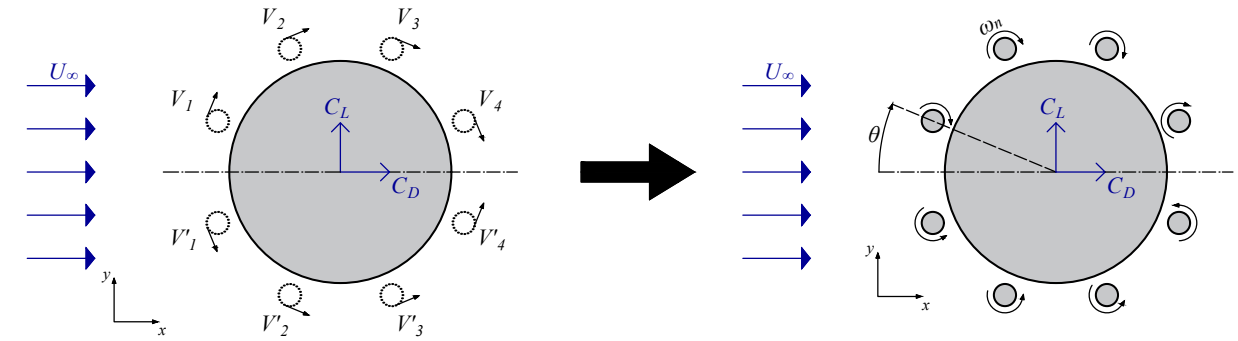
 $\omega'_n = -\omega_n$ for the lower rods. In order to speed up or lower the rotation rates, while keeping their proportionality, the control variable ζ was employed. This parameter adopted values $\zeta = 0.0$ (passive rods), 0.5, 1.0, 1.5, 2.0 and 2.5 in our analysis. Of course, to impose $\zeta = 0.0$ rendered the system completely passive; and $\zeta = 1.0$ in case 1 imposed the potential-flow velocities. Physical meaning can be attributed to ζ only in case 0, as it coincided with the ratio of the rods' velocities by the incoming flow.

Such definition of the velocities refers to the case hereby denoted case 1. Another setup, related to case 1, with the same input kinetic energy, is henceforth denoted case θ . The two cases were hereby related in the following manner to constrain the same input kinetic energy to spin the rods:

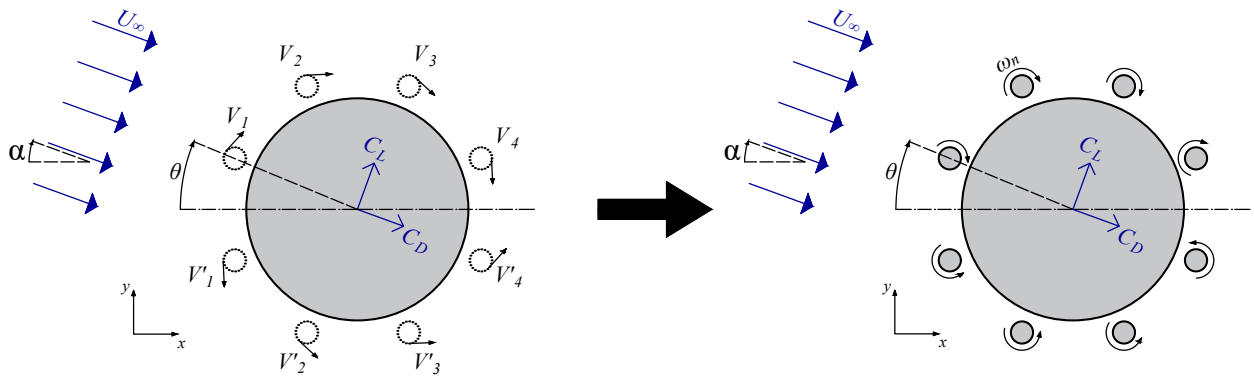
$$\left[8\omega_0^2\right]_{\text{case }0} = \left[\sum \omega_n^2\right]_{\text{case }1} \tag{6}$$

to find ω_0 for each ζ (since ω_n is a function of ζ). Figure 5 summarises the explanation above and emphasises that the update of the velocities of the rods depended both on their position θ_n and on the angle of attack of the incoming flow α .

For physically-meaningful results, for a given angle of attack and set of rotation speeds, the simulations were advanced with time steps that were limited by three conditions: i) a maximum Courant number below 0.99 in each simulation, ii) at least 70 parts of the revolution of the rods, and iii) 100 parts of a cycle of vortex shedding were captured (the cycle here corresponds to that defined by the flow over a bare cylinder, see section 3.1). It must be noted that since the Reynolds number based on the rods' dimension is $Re_d = U_{\infty}d/\nu = 5$, vortices were not emanated by them



a) Zero angle of attack, $\alpha = 0^{\circ}$



b) Non-zero angle of attack, $\alpha \neq 0$.

Figure 5: Velocities V_n , V'_n , $n=1,\ldots,4$ stemmed from the potential-flow field about a plain cylinder (without the wake-control device). In the left subfigures, dotted lines emphasise that the rods were not placed in the flow. These velocities were computed at points specified in radial coordinates by r=R=D/2+G+d. For the angular coordinate, in (a) $\alpha=0^\circ$, $\theta_n=\pm22.5^\circ\pm45^\circ(n-1)$; and (b) $\alpha\neq0^\circ$, $\theta_n-\alpha$ were used. In case 1, the angular velocities for the system were given by $\omega_n=\zeta V_n/(d/2)$ (see right subfigures, where the rods were fitted to the main body, thus the unbroken lines). In case 0, $|\omega_n|=|\omega_0|$ and $8\omega_0^2=\sum\omega_{n,\mathrm{case}\ 1}^2$ for each ζ .

(and we can emphasise that even for low $Re \gtrsim 45$, according to Mittal and Kumar, 2003, the rotation mechanism would still eliminate vortex shedding).

Further details of the finite volume method employed in the present work are described in Carvalho (2023), and Moukalled et al. (2016) for OpenFOAM implementation details; an analogous numerical scheme, with minor differences, is found in Carvalho and Assi (2023a).

Table 1: Mesh convergence study in terms of mean drag $(\overline{C_D})$ and root mean square of lift (\hat{C}_L) . Quantities between parentheses represent the percentage change from the respective mesh relative to the most refined case. We highlight the row of the grid used in this work.

Number of cells	$\overline{C_D}$		\hat{C}_L	
83,760	1.469	(0.36%)	0.2759	(0.29%)
110,000	1.473	(0.09%)	0.2771	(0.73%)
123,120	1.473	(0.10%)	0.2808	(2.07%)
132,880	1.473	(0.12%)	0.2778	(0.98%)
143,568	1.472	(0.15%)	0.2767	(0.58%)
146,480	1.473	(0.12%)	0.2776	(0.91%)
174,000	1.474	(0.05%)	0.2768	(0.62%)
179,088	1.474	(0.05%)	0.2748	(0.11%)
185,920	1.474	(-)	0.2751	(-)

3. Results

3.1. Grid independence and verification

A grid independence study was performed prior to varying the angle of attack and the rotation speeds of the system through α and ζ . Simulations included the reference configuration of the passive system at null angle of attack of the incoming flow. Each simulation was left to run for $40T_S$, where $T_S = 1/f_S$ corresponds to the inverse of the vortex shedding frequency (f_S) of a bare cylinder in laminar regime, usually defined by the Strouhal number $S_t = f_S/(U_\infty/D)$, and reasonably approximated in this regime by $S_t \approx 0.2$ (Norberg, 2001). The results are shown in table 1. Significant changes neither occurred in mean drag $(\overline{C_D})$ nor in root mean square (RMS) of lift (\hat{C}_L) with increased refinement of the mesh. Even for \hat{C}_L , the greatest change was of 2.07% for the mesh with 123,120 cells relative to that with 185,920.

The highlighted O-grid mesh of table 1 was verified with the unstructured grid of (Carvalho et al., 2021, which is not O-grid shaped), with the following results: our $\overline{C_D}$ was 3% and \hat{C}_L was 9.7% below that of the previous work. We also ran this simulation with the (non-O-grid-shaped) structured grid of Carvalho and Assi (2022) for the present Re. The differences found were of 3.2%

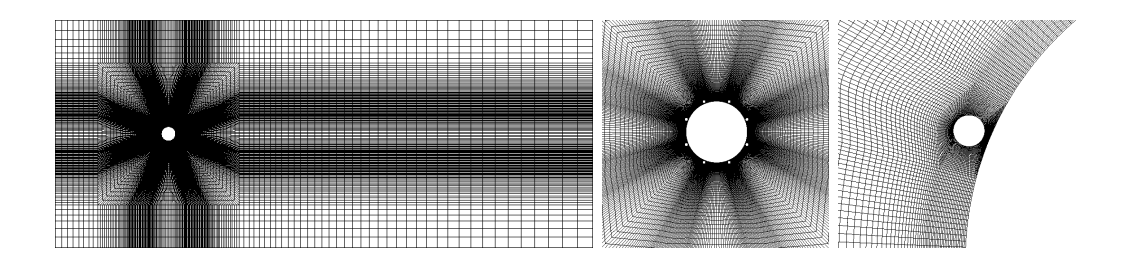


Figure 6: Another mesh used for verification. It entailed the same size of the cell near the wall and low grid refinement ratios, encompassing 72,910 cells and maximum aspect ratio of 25.

and 3.3%, respectively. For yet another mesh (see figure 6) the differences were below 3%, even for $\zeta = 0.5$ and $\zeta = 1.0$. The latter mesh was submitted to a verification test by the authors and compared with that of Carvalho et al. (2021) with comparably good results. Validation was not made because experiments have not been conducted for the present system and Re at present.

Considering that the mesh of this work and those above differ qualitatively, the present gridindependence and verification results are judged satisfactory, particularly because we are more concerned with the trend of these coefficients rather than with their single value considered alone.

3.2. Time histories

Combinations of α and ζ were run in parallel for $40T_S$ for appropriate convergence, which was generally attained after $16T_S$. Time histories of C_D and C_L are plotted together in figures 7a and 7b for cases 0 and 1, respectively. For clarity, only the curves corresponding to $\alpha = 0^{\circ}$, 10° , and 20° are shown as examples, but all angles of attack mentioned in section 2.1 were run as just explained. Figure 7a remarks that in case 0 the parameter ζ matched the ratio of the linear speed applied to the rods $(U_c = \omega_0 d/2)$ to the far-field incoming flow (U_{∞}) . This association is not valid for case 1.

Amongst similarities between the two plots, it becomes clear that, given enough rotation speed, the control rods disrupted vortex shedding, observed as a reduction of the fluctuating lift. For $\alpha = 0^{\circ}$ the amplitude of the lift coefficient was shortened in approximately 4 times from the passive setup to the less energetic configuration with $\zeta = 0.5$. The magnitude of C_D also fell monotonically with the faster spinning of the rods.

Despite these similarities, notably about drag, the two plots show very different behaviours for $\alpha \neq 0^{\circ}$. Whereas the entire system of case 0 was subjected to strong directional effects in the form of non-zero mean lift – the greater the angle of attack, the greater was the absolute value of the mean lift –, case 1 was generally insensitive to the effect of α , making up for a "more

omnidirectional" control arrangement. We highlight that by *omnidirectionality* we refer here to the feature that the system was able to counteract vortex shedding and reduce hydrodynamic loads, qualitatively, in the same fashion as it would under different α .

Besides, vortex shedding suppression for $\alpha = 20^{\circ}$ only occurred at $\zeta = 1.5$ in case 0, instead of $\zeta = 1.0$ as in case 1. Therefore, not only case 0 was more susceptible to lift growth due to increasing α , but it also required greater input kinetic energy (as it can be directly associated with ζ) than case 0 to fully eliminate vortex shedding at higher angles of attack. In addition, for the present range of values of ζ and α , case 0 showed ever greater lift with the increment in any of these two parameters, provided $\alpha \neq 0^{\circ}$.

3.3. Vortex contours

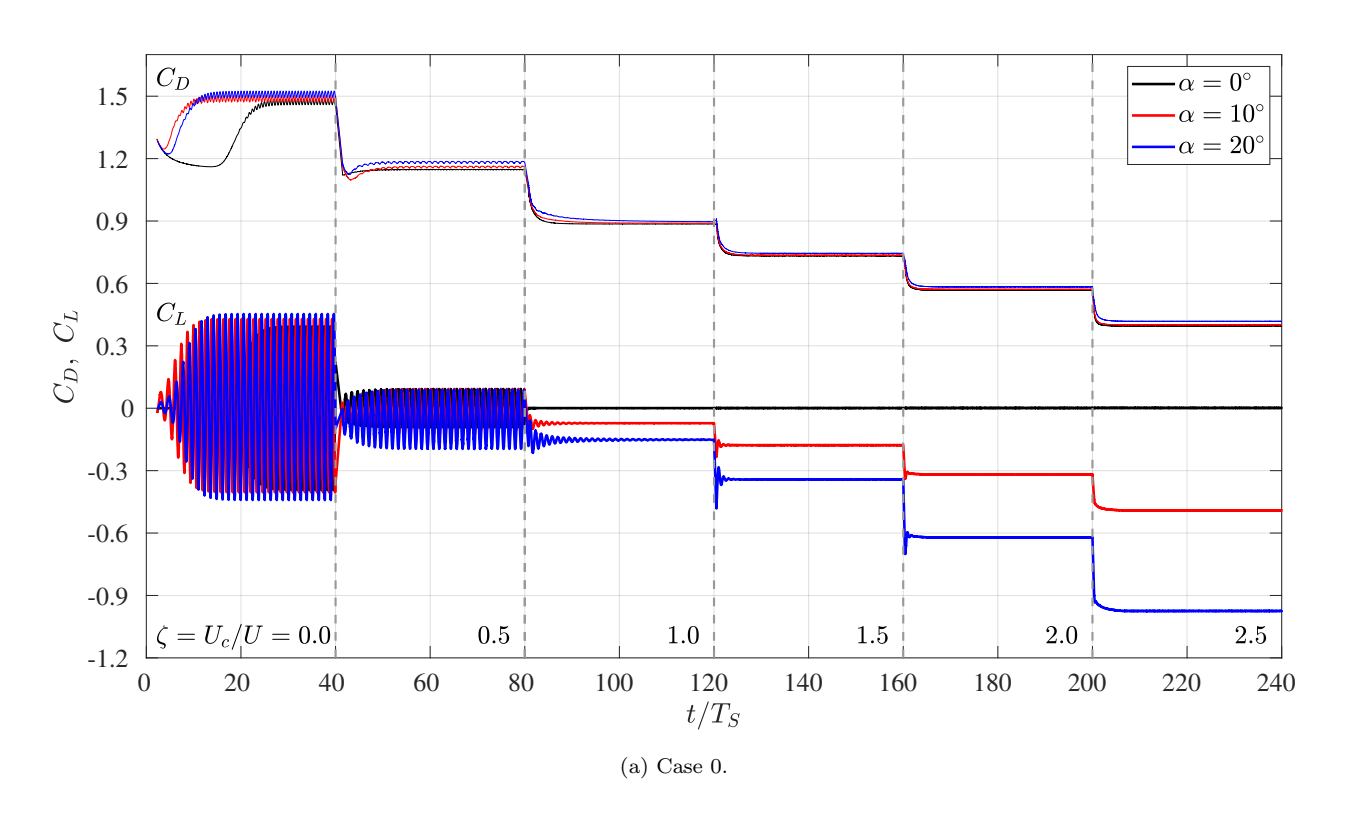
Instantaneous contours of the z-vorticity component are depicted in figure 8, where the snapshot formed by row and column corresponds to a different combination of ζ and α , respectively.

The lines portraying $\zeta = 0.0$ and $\zeta = 0.5$ of figure 8a clearly show an instant in which the blue vortex (negative vorticity) was on the onset of shedding. The figure also shows the directional effect, because the wake was aligned with the direction of the incoming flow. It is worth noting that, in spite of the wake topology shown for $\zeta = 1.0$ in figure 8a – which does not allow one to properly visualise vortex shedding –, the oscillation in lift, detected in the corresponding time history of figure 7, reveals that remaining vortex shedding was still present in this configuration.

For higher values of ζ , the vorticity fields corroborate with the preceding time history in that vortex shedding was completely eliminated. Nevertheless, another detail is added: an imbalance occurred between regions of negative (blue) and positive (red) contours within the wake, meaning that a non-zero steady lift was generated.

The fourth row of figure 8a ($\zeta=2.0$) shows that the magnitude of vorticity of the red region grew ever greater compared with that of the blue region, the more the incoming flow was subjected to higher values of α . For $\zeta=2.0$ and $\alpha=20^\circ$ (last column and last row of figure 8a), there were many more contours within the positive-oriented part compared with its blue counterpart (for a symmetrical range of vorticity contours, $\omega/(U_\infty/D)=[-1,1]$). This indicates that in the vortical composition of the wake, a larger anticlockwise-oriented vorticity region was formed.

This correlates well with the progressively greater lift (in absolute value) pointed out by figure 7. Because the stronger vortex formed past and below the entire system not only produced an



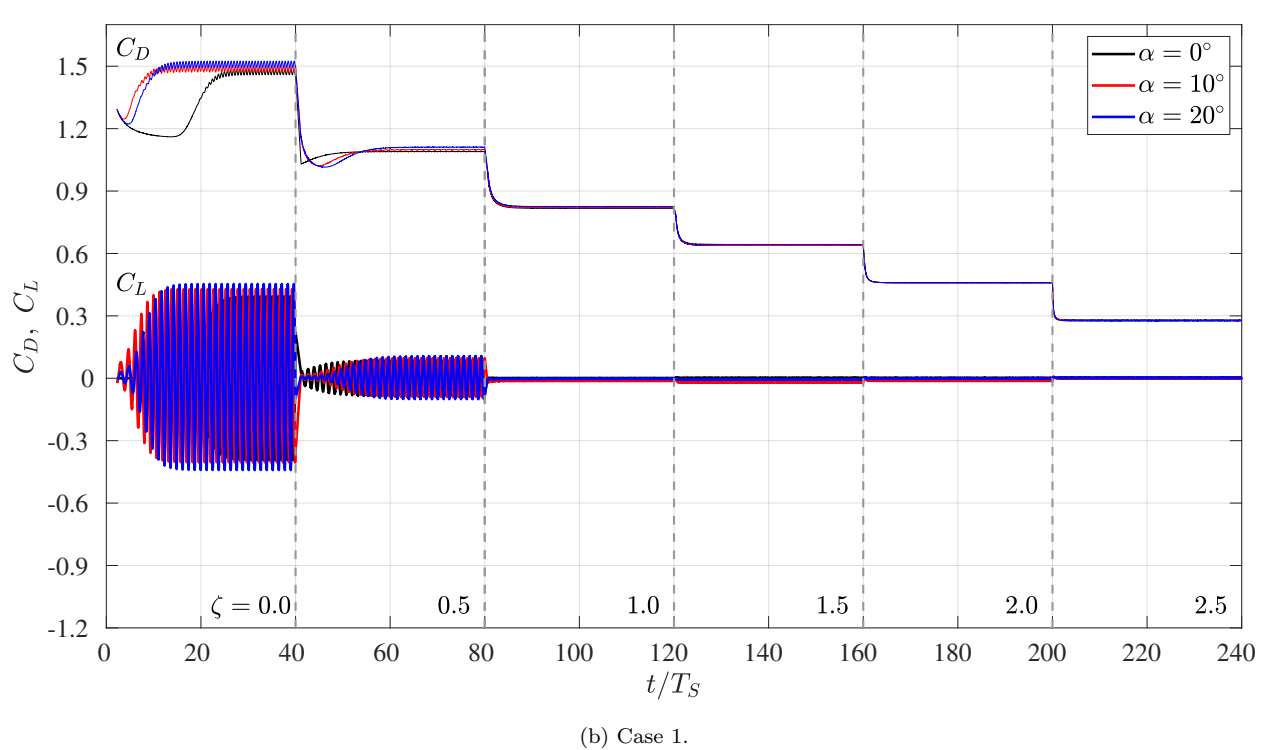


Figure 7: Examples of time histories of drag and lift coefficients for cases 0 and 1.

Table 2: Inclination of \hat{C}_L relative to α for different ζ .

ζ	$\tan^{-1}(\hat{C}_L/\alpha)$
0.0	-0.0097
0.5	0.14
1.0	0.38
1.5	0.87
2.0	1.6
2.5	2.5

imbalance between the two parts, but further created a region of even lower pressure, the resulting lift was directed downwards and it was greater in magnitude than other corresponding cases of lower α .

A similar behaviour was noted in case 1 for low ζ values and $\alpha=0^\circ$ (first column and first rows of figure 8b). However, as the rotation speeds were set according to potential flow for every angle of attack, the symmetry in the vorticity contours prevailed even for configurations of high ζ and α concurrently. The net effect was to zero mean and instantaneous lift. To render this point clearer, figure 9 compares cases 0 and 1 for $\zeta=2.5$ and $\alpha=20^\circ$, and shows that there are far more vorticity contours in case 0 on one side than on the other relative to the direction of the incoming flow, and compared with case 1.

3.4. Force coefficients upon the entire system

Coefficients of mean drag $(\overline{C_D})$ and root mean square (RMS) of lift (\hat{C}_L) are given in figure 10. Lift was one order of magnitude lower in case 1 than in case 0. Therefore, to ensure a better visual-isation of its behaviour, the RMS of lift coefficient was multiplied by 25 in figure 10b. In agreement with and complementing the time histories of figure 7 for other angles of attack, figure 10a shows that the mean drag acting on the entire system was generally weakly influenced by changes in α .

Contrarily, however, the resulting RMS of lift of case 0 was affected monotonically by the angle of attack, as demonstrated by figure 10b. Furthermore, the figure reveals that the greater the rotation speeds were (as given by higher ζ), the greater were the inclinations of the curves \hat{C}_L vs α , as exposed by table 2.

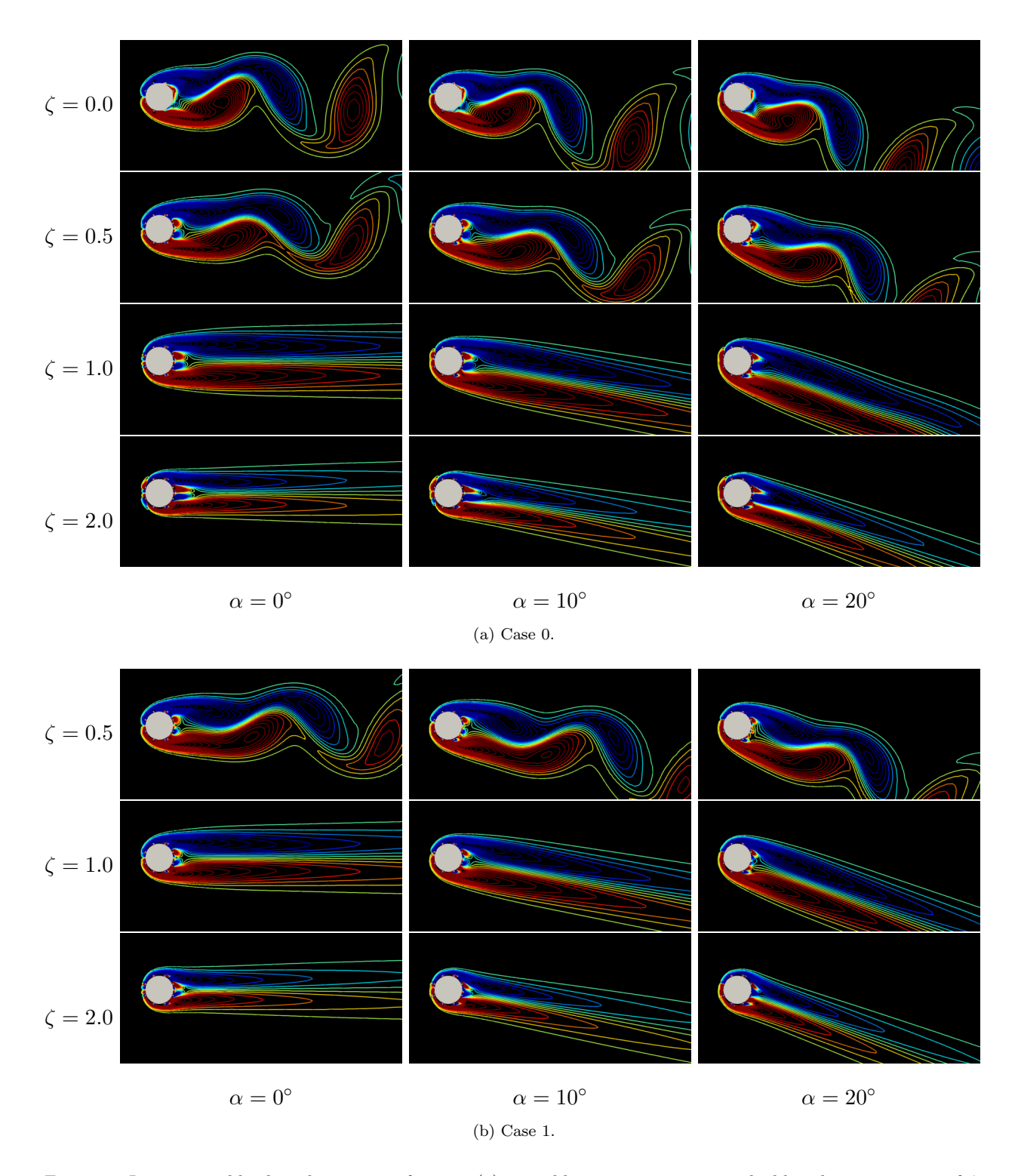


Figure 8: It is noticeable that the system of case 0 (a) was able to suppress vortex shedding later, in terms of ζ , than case 1 (b). The former portrayed an unsteady wake for higher ζ depending on α , than the later, which achieved this result for $\zeta = 1.0$ regardless of α . Since both cases possessed the same input kinetic energy for a fixed ζ , case 1 presents a more effective solution to suppress vortex shedding with economical energy expenditure.

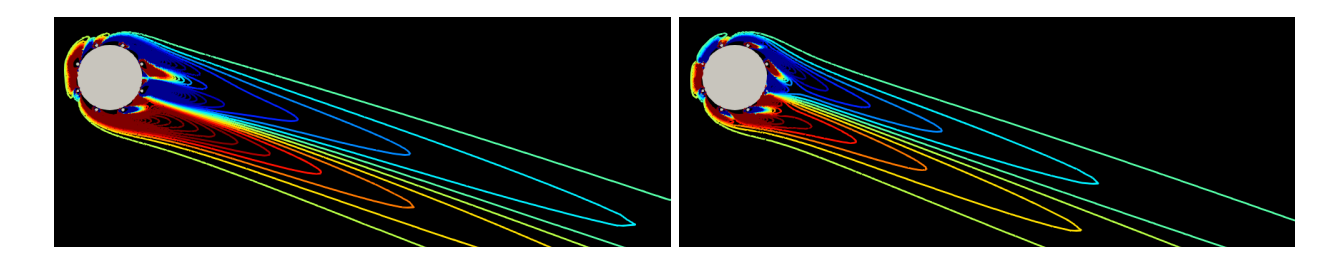
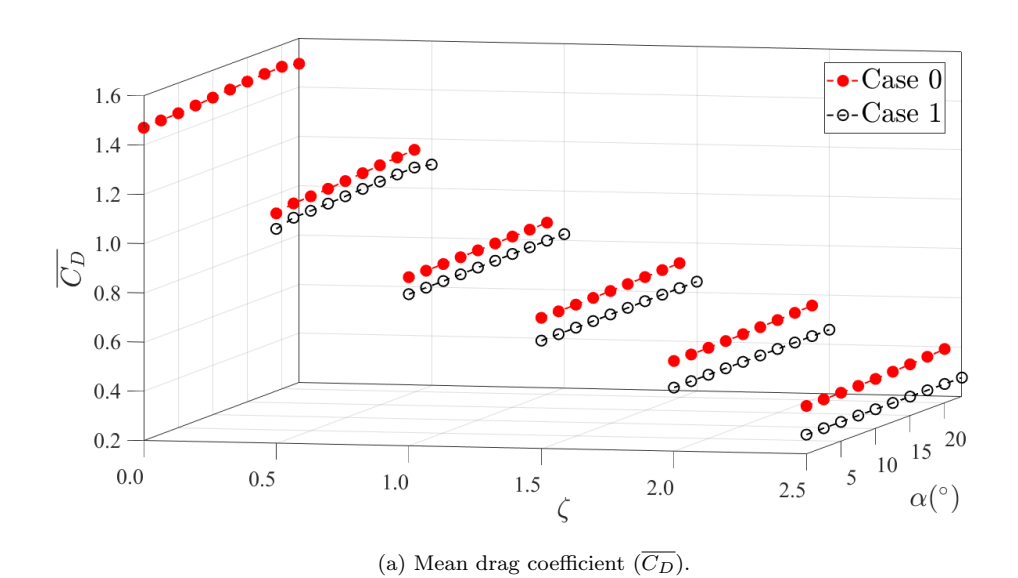


Figure 9: Vorticity contours of cases 0 and 1 for $\zeta = 2.5$. An imbalance was produced between negative (blue) and positive (red) contours of z-vorticity in case 0 that was not present in case 1.



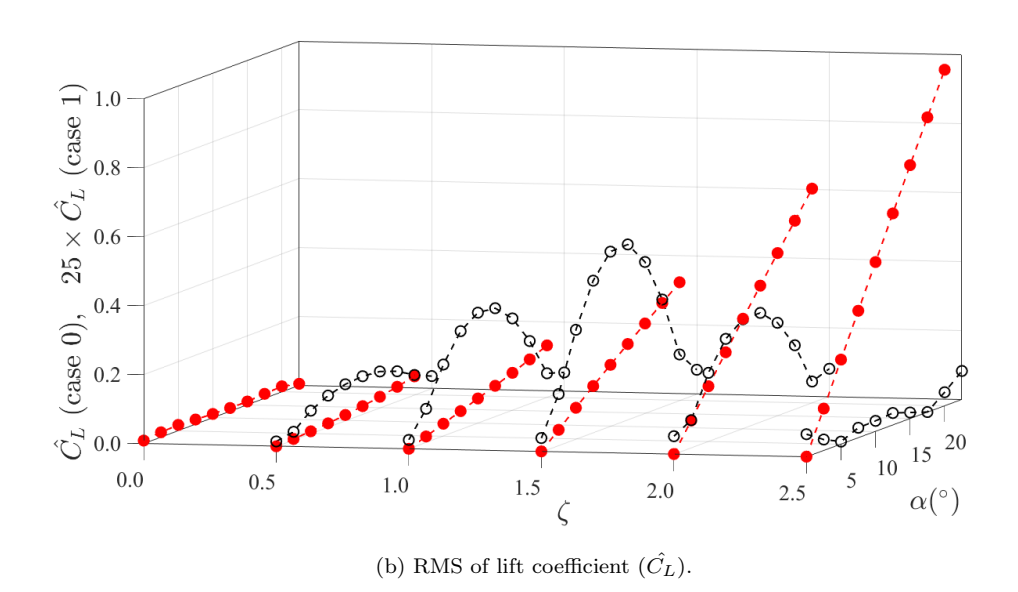


Figure 10: Hydrodynamic forces acting on the entire system for cases 0 and 1.

For case 1, the \hat{C}_L -curves of figure 10b behaved in a parabolic-like fashion, achieving greatest value at $\alpha = 10^{\circ}$, except for $\zeta = 2.5$, where highest values were concentrated at the extremes $\alpha = 0^{\circ}$ and $\alpha = 22.5^{\circ}$. Nonetheless, for this level of rotational speeds this different pattern cannot be considered to be physically meaningful, because the lift is negligible (despite the fact that the lift of this plot was multiplied by 25).

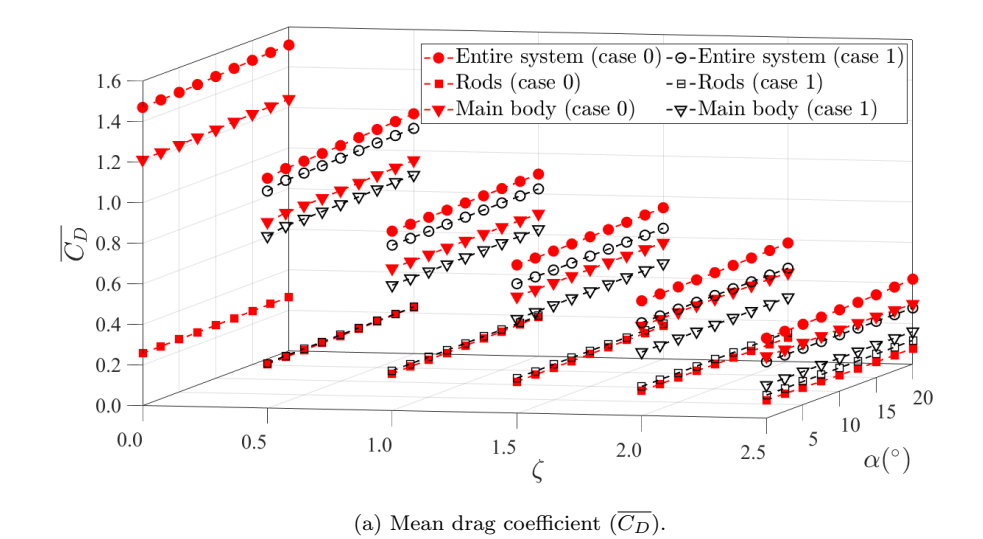
In order to discern whether the aforementioned directional effect stemmed from the entire system, collectively from the rods or from the main body, figures 11a and 11b decompose the mean drag and the mean lift for each of these structures.

In both cases, the previous claim regarding the lack of sensitiveness of the mean drag relative to the angle of attack is supported by figure 11a. For the mean lift, it becomes clear from figure 11b that the rods were generally oblivious to the angle of attack for small ζ in case 0. This behaviour differed as ζ adopted greater values. While in case 0, for a fixed ζ , the curves of $\overline{C_L}$ formed a straight line, in case 1 these curves resembled a curved shape.

For the entire system and for the main body of case 0 a steep decrease occurred in the mean lift toward more negative values as α increased. Furthermore, there was a difference in slope between the $\overline{C_L}$ -curve for the entire system and for the main body. Generally, $\overline{C_L}$ reduced faster for the entire system compared with that for the main body, justified by the presence of the rods. Therefore, because the rods were progressively affected at higher ζ by the angle of attack, their presence led to a strongly directional system in case 0.

In addition, figure 11 calls attention to the fact that the root of the non-directional behaviour of case 1 was directly related to the way that the rods' speeds were determined, highlighted by figure 12. By adapting the rotation speed according to the potential flow for different angles rendered the system essentially omnidirectional. Furthermore, the system was "more omnidirectional" the greater was the value of ζ in case 1, translated into a flattening effect upon the $\overline{C_L}$ -curves observable in figure 13.

The opposite tendency was followed by case 0, proving that to impose a uniform rotation speed to all rods gave rise to an imbalance of lift that was not mitigated by feeding the entire system with a larger amount of kinetic energy. Rather, to diminish or eliminate hydrodynamic loads, each rod's rotation is expected to be weighted properly within the entire setup, to contribute significantly according to the angle of attack of the incoming flow, and depending on its relative



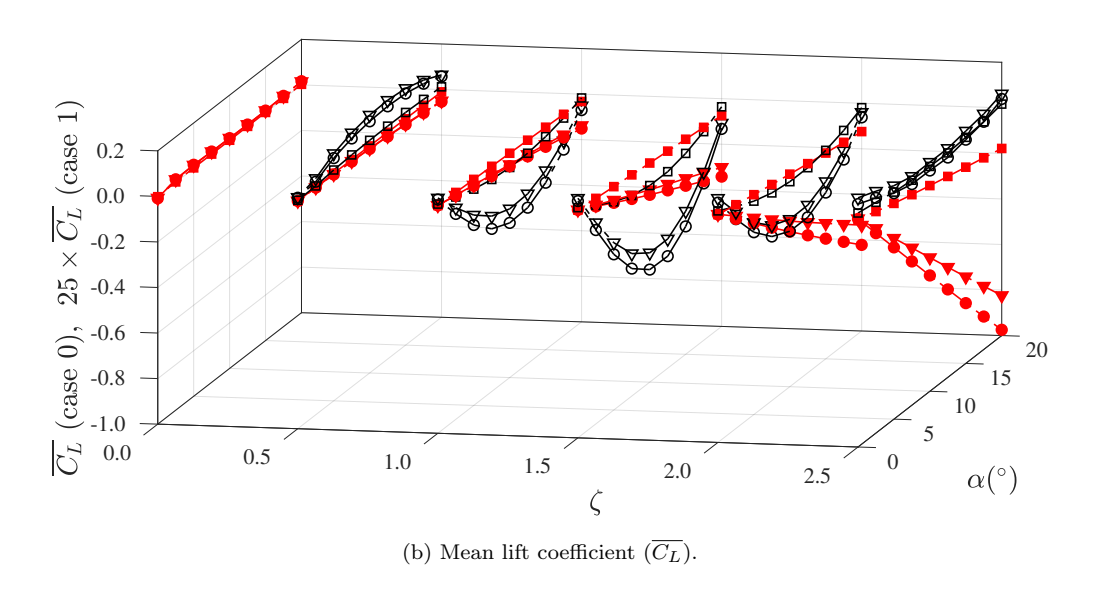


Figure 11: Mean hydrodynamic forces acting on the main body, on the rods and on the entire system for cases 0 and 1.

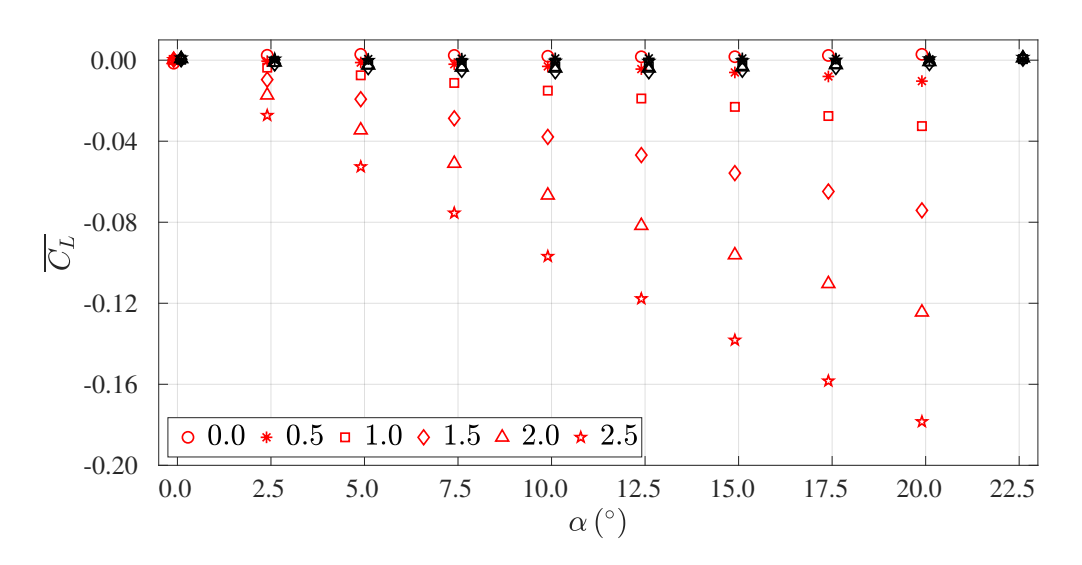


Figure 12: Resultant lift $\overline{C_L}$ from the collective effect of the rods of cases 0 (black) and 1 (red). Strikingly different behaviours justify the omnidirectional quality of each system.

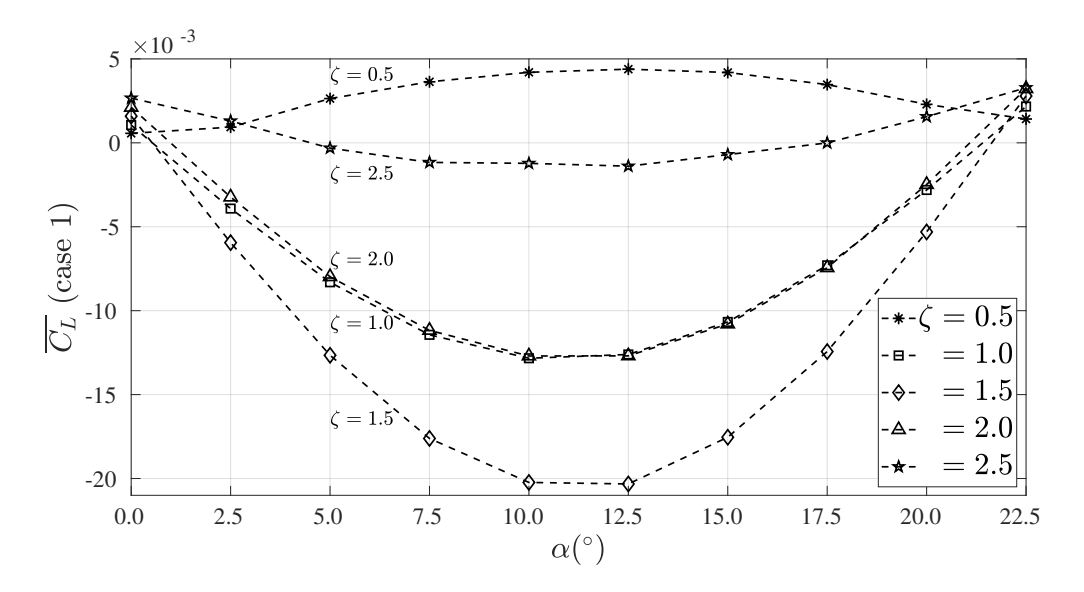


Figure 13: A flattening effect on the curves of the mean lift distribution $\overline{C_L}$ with α on the entire system of case 1 indicates a tendency where the angle of attack α becomes less important with growing rotation speeds.

position with respect to the boundary layer and to the wake.

3.5. Loads applied to the rods

Figures 14 and 15, respectively, present the mean drag and the mean lift acting on each rod for a subset of the α -values investigated in this work. For each of these values, different markers were assigned to convey the effect of the rotation speeds through ζ . The reference configuration of $\alpha = 0^{\circ}$ was inserted on top of the respective figures. This section is focused on the quantitative side of the hydrodynamic coefficients, to allow the interested reader to compare with previous papers of this context (see Mittal, 2001; Korkischko and Meneghini, 2012; Assi et al., 2019; Carvalho and Assi, 2023a, and references therein). The reader whose concern leans toward the qualitative analysis may move on directly to section 3.6.

In terms of mean drag, figure 14a shows that case 0 remained broadly similar to its reference case of figure 14 with $\alpha=0^\circ$ with the increase in rotation speeds, with bias toward the lower rods (for negative θ , see figure 1 for the convention) which were weighted with greater loads. Amongst these rods, P_2' showed the greatest decrease toward a zero value with larger ζ , although this rod was not within the most representative of the system. Upper rods ($\theta>0$) P_1 and P_4 were subjected to generally lower loads as the incoming flow arrived to the system at higher slope α . Conversely, P_2 developed greater absolute values; while the mean drag on P_3 progressively collapsed to a single value of approximately 0.07 regardless of ζ , pointing to an independence of this parameter at sufficiently high α . Due to these changes – in particular due to those of P_1' , P_1 and P_2 , which became all negative with increasing ζ at any of these angles of attack – case 0 was able to partially counteract pressure drag.

Now we turn to the analysis of the mean drag upon the rods of case 1, figure 14b, where the difference of the general tendencies of the dashed lines with respect to the $\alpha=0^{\circ}$ case is strikingly evident. For $\alpha>0$, the loads on P_1 , P_3 , P_2' and P_4' presented a steady tendency of collapsing to a single value, as it can be perceived from top to bottom of figure 14b. This set of rods at $\alpha=20^{\circ}$ behaved rather symmetrically, with symmetrical pairs given by (P_1, P_4') and (P_3, P_2') , that come from the definition of the potential-flow velocities, which is clearly different from the reference case. As a matter of fact, taking into consideration $\alpha=20^{\circ}$ of figure 14b, for $-112.5^{\circ} < \theta < 112.5^{\circ}$, the plot is mirrored about 22.5° . Furthermore, the overall mean drag on the system was essentially attenuated by P_2 and P_1' .

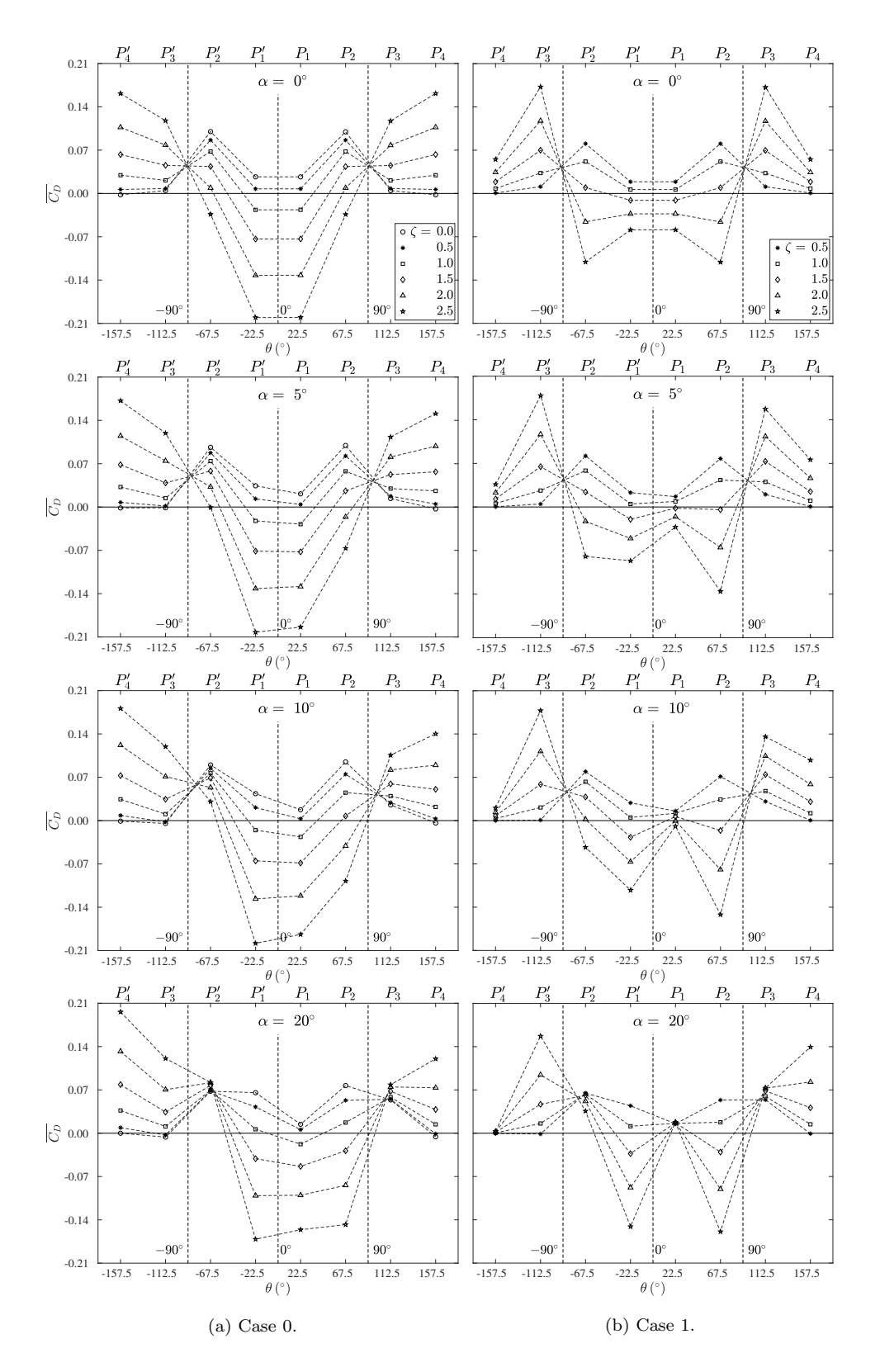


Figure 14: Mean drag acting on each rod for different angles of attack.

In terms of mean lift applied to individual rods, only slight differences were observed between cases 0 and 1 as seen in figure 15, when compared to the same analysis for the mean drag, and did not stray away from the reference of $\alpha = 0^{\circ}$ of each respective case (see figure 15). Figures 15a and 15b resemble one another in the following features: i) the load applied to P_1 zeroed as the angle of attack grew, ii) the loads on P_2 and P'_3 reduced in magnitude, while those on P_3 , P_4 and P'_2 amounted to higher levels; iii) the force applied to P'_1 grew much faster for higher α (indeed, for $\alpha = 5^{\circ}$, changes in ζ did not alter significantly the load applied to P'_1), while that on P'_4 became insensitive to rotation. The difference between the two cases lied essentially in the greater magnitude of the loads in case 1 against case 0.

As aforementioned, case 1 was able to completely eliminate the mean lift, even at the higher angles of attack of the present analysis. Contrarily, case 0 revealed a much "less omnidirectional" quality. As far as lift was concerned, the nuance in these different behaviours allude to the fact that for case 1 there was a rapid increase in this load component exerted on P_3 ; concomitantly, this configuration reduced the mean lift on P_2 . For case 0 this sequence of events occurred for more advanced values of α . The load on P_3 only surpassed that on P_2 for case 0 at $\alpha = 20^{\circ}$, while for case 1 this occurred at $\alpha = 10^{\circ}$, as disclosed by figure 15a. Another supporting aspect is that the contributions to the mean lift of the rods for $\theta < 0$ showed lower magnitudes compared with those for $\theta > 0$. Thus, on average, the system of case 1 employed an upward force that counteracted that promoted by the incoming flow, directed downward. This last point is further explored in section 3.7.

3.6. Hydrodynamic coefficients applied to the cylinders and to the entire set

Figure 16 qualitatively exhibits the resultant force applied on each cylinder (coloured) and on the entire system (in greyscale) at different angles of attack of the incoming flow (with direction pointed by the dark blue vector on the left, emphasised by the dashed line). Figure 16a exemplifies the reference case of $\alpha = 0^{\circ}$. For clarity, the loads applied to the rods located at y < 0 were omitted.

The sequence of figures of case 0 singles out that, although the collective contribution from the rods was virtually insensitive to the incoming flow at low angles of attack (as supported by the previous section), each rod was acted upon by resultant forces that were indeed influenced by ζ at sufficiently high α . Overall, in both cases the forces acting on the rods P_2 and P_4 changed little

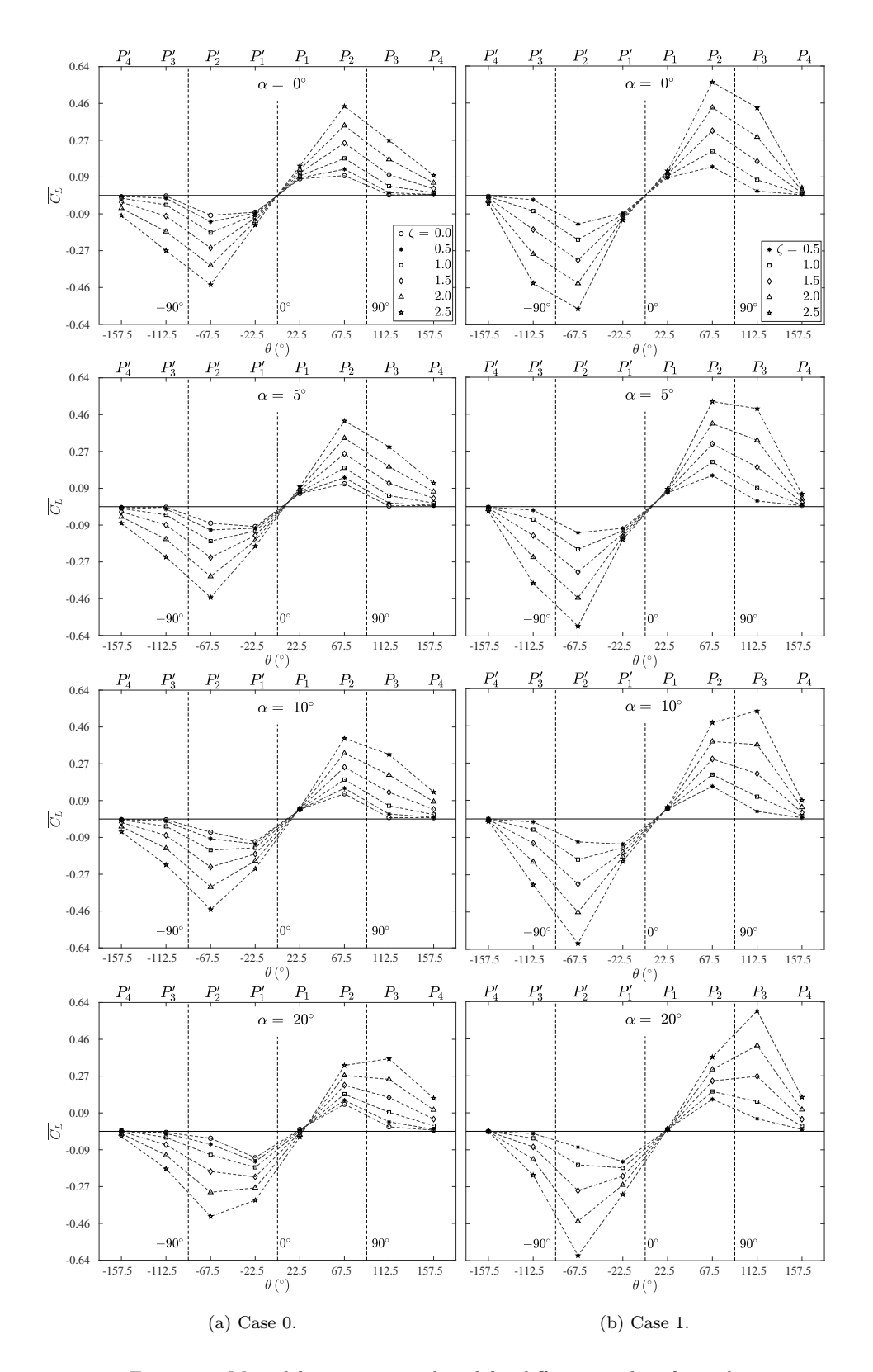


Figure 15: Mean lift acting on each rod for different angles of attack.

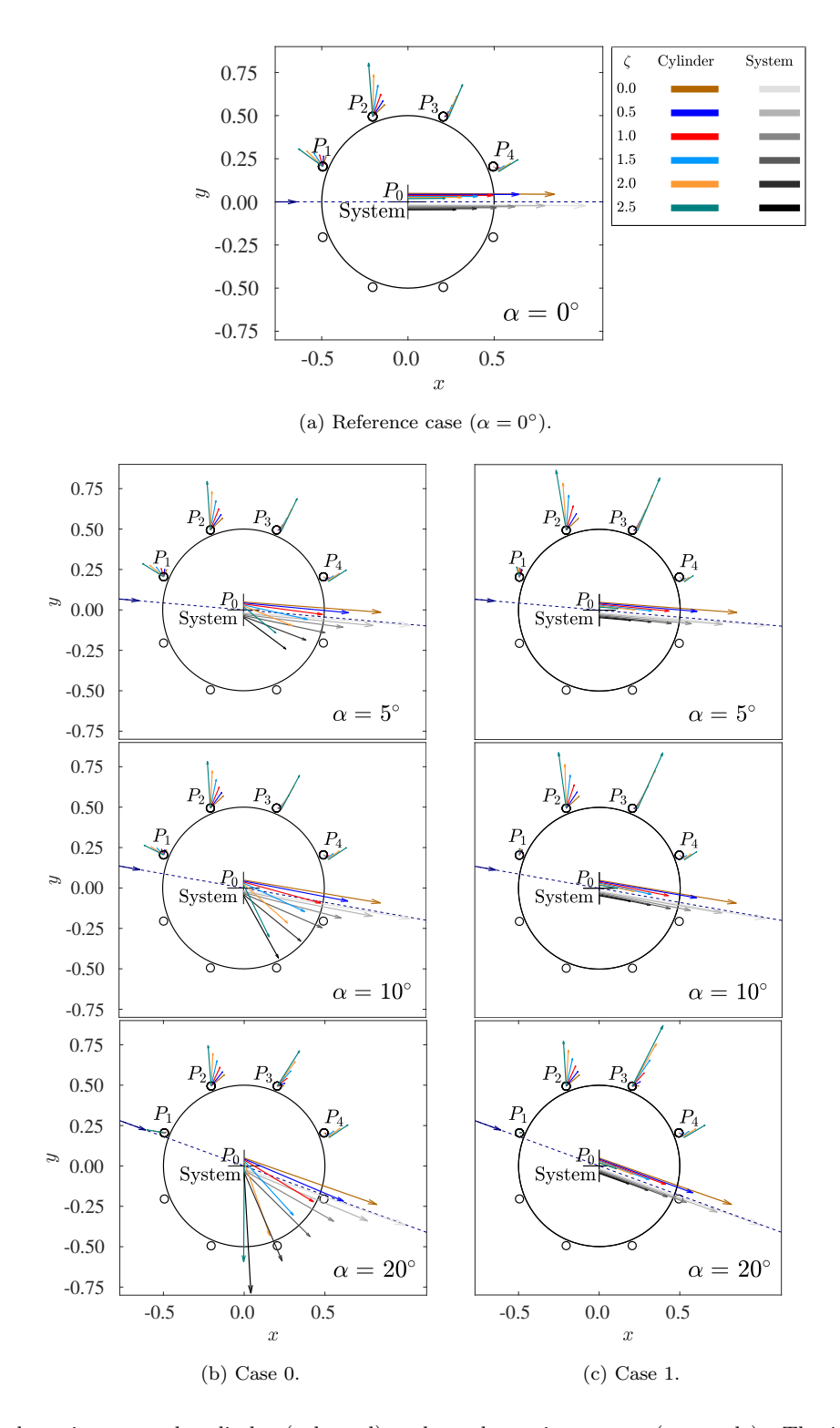


Figure 16: Loads acting on each cylinder (coloured) and on the entire system (greyscale). The incoming flow is represented by the dashed line and the respective vector. The resultant force applied to the main cylinder was slightly moved from the centre of the body, to avoid confusion with that acting on the entire system.

in direction and magnitude with α ; oppositely, the loads applied on P_1 and P_3 were remarkably altered with α .

We first consider the change of the loads with respect to α for cases 0 and 1. For P_1 it is notable that with higher α the resultant forces became smaller and their directions were modified gradually until $\alpha = 20^{\circ}$, when the forces for each ζ aligned approximately in the same direction as that of $\zeta = 2.5$, except for the loads corresponding to $\zeta = 0.0$ and 0.5. In general, for this angle of attack the loads on P_1 diminished to an almost imperceptible size for different ζ . For P_3 the contrary pattern was followed. For a fixed ζ , as α varied, so did the direction of the load applied to this rod. Collectively, the loads organisation went from a parallel alignment at different ζ when $\alpha = 0^{\circ}$ to evidently diverging directions when $\alpha = 20^{\circ}$.

Now we investigate the effect of ζ upon the resulting loads. Taking into consideration the orientation of the resultant force with ζ (for fixed α) of figures 16b and 16c, it can be perceived that with greater angular speeds, the load upon P_1 inverted in the x-direction. With the inversion of its x-component, the load on P_1 started to counteract part of the pressure drag that resulted upon the system due to its obstruction to the incoming flow. Analogously, P_3 opposed the otherwise downward lift as it produced an increasing upward load. For sufficiently large α , it also became evident that the load on P_3 gradually oriented further away from the positive x-direction with the increase in ζ , leaving a more horizontal configuration toward a steeper one. A shift in its x-component did not occur as it happened for P_1 for this range of ζ . Nevertheless, this gradual change in orientation might call attention for increasingly higher speeds, as it may be lead to propulsion of the entire system akin to that investigated by Silva-Ortega and Assi (2017b).

It may be noted from figure 16a that most of the loads were concentrated in magnitude on P_2 and P_3 , a tendency that persisted for and became more evident with larger α in cases 0 and 1.

In spite of the commonalities, discrepancies can be noted between cases 0 and 1. The omnidirectional property of case 1 stands out in figure 16c compared with case 0 of figure 16b. Indeed, case 0 was prone to significant lift production as α departed from null value, that is, from its most symmetrical setup relative to the incoming flow. This feature led the two cases to an astounding distinction: Even though both cases reduced drag, only case 1 was capable of eliminating lift. This can be inferred from these qualitative figure. Primarily due to the much larger loads supported by P_2 and P_3 , the resulting forces applied on the entire system in case 1 were well aligned with the dashed line representative of the incoming flow, in clear contrast with case 0. It is worth noting, of course, that case 1 also reduced drag beyond case 0.

3.7. Resultant forces

The previous analysis is now complemented with quantitative results. Figure 17 exhibits the resultant force acting on each rod for both setups herein analysed, for an economical number of plots. Nevertheless, the tendency that is described below was observed for the entire range of α exhibited in section 2. Each group of bars is associated with a pair of rods that were antisymmetrically placed relative to the incoming flow (and thus their rotations were of the same magnitude, given by potential-flow theory). Antisymmetry here is characterised by the rods whose centres were positioned at the same angle relative to the dashed line, e.g., the pairs P_1 and P'_4 , P_2 and P'_3 , etc., provided $\alpha > 0$.

From this figure, it can be detected that there was a gradual decrease in the load upon P_1 , P'_4 as α adopted larger values, especially for the fastest rotation rates. As α reached 22.5° (omitted here for brevity), their velocities were set to null value, according to our potential-flow analogy, that led these rods back into a passive behaviour. In this setup, these rods bore virtually negligible loads. The same pattern occurred for rods P_2 , P'_3 although these rods were kept active throughout the different angles of attack. Oppositely, the pairs P_3 , P'_2 and P_4 , P'_1 followed an upward tendency of the resultant forces. Essentially, these two pairs offset the contribution from the former pairs, that decreased.

Cases 0 and 1 essentially followed the same tendency. The difference was concentrated on the adaptability of the system in interacting with the incoming flow. Changes in case 1 advanced much faster, in terms of α , than in case 0.

3.8. Power-loss

It is well known from the work of Korkischko and Meneghini (2012) that increasing the speeds of the rods indefinitely promotes reduction in the mean drag and lift for $\alpha = 0^{\circ}$. From the paper of Shukla and Arakeri (2013) one can analyse an active system, such as the present, from the point of view of power expended to mitigate the mean drag $\overline{C_D}$ and to counteract the mean shear $\overline{C_N}$ cumulatively into a power-loss coefficient $\overline{C_{PL}}$ as the rods rotated about their respective axes, with the following expression

$$\overline{C_{PL}} = \overline{C_N} + \overline{C_D} \tag{7}$$

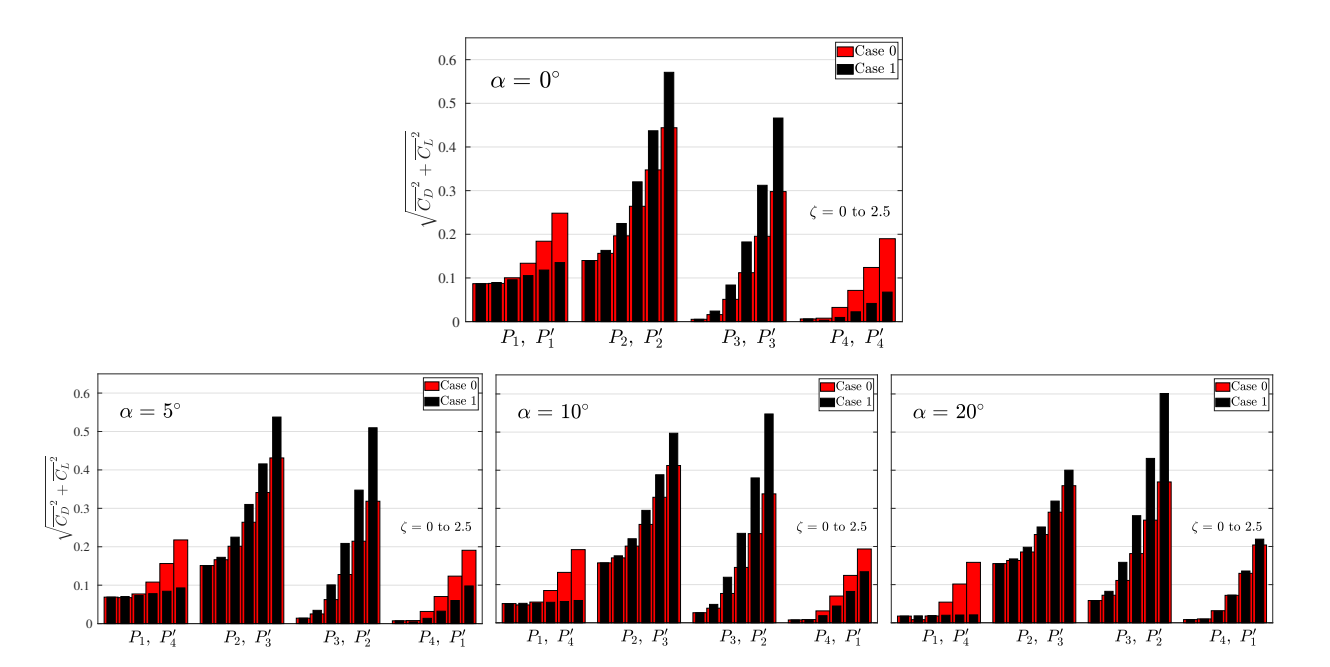


Figure 17: Resultant loads on the rods for different angles of attack. Groups of bars associated to each rod correspond to ζ varying from 0.0 to 2.5 in steps of 0.5. The indicated pairs of rods for each group of bars have symmetrical $(\alpha = 0^{\circ})$ or antisymmetrical loads $(\alpha \neq 0^{\circ})$ with equal magnitude.

where C_N is given by the integration of the shear stress (τ_n) over the surface of the rods to account for the power spent to keep their rotational motion against viscous traction

$$C_N = \sum_{n=1}^{8} \frac{p_n}{\rho U_{\infty}^3 D/2},\tag{8}$$

and

$$p_n = U_n \int_0^{2\pi} \tau_n(\theta) \, \frac{d}{2} \, \mathrm{d}\theta, \tag{9}$$

written in time-averaged form (the bar placed over the variables indicates mean values). With this relationship, the system of cases 0 and 1 can be compared. Equation 7 can also be used to compare active systems with a passive one, e.g., the system with (passive or spinning) rods and the bare cylinder. We noted that to subject the entire system to different angles of attack did not output significant difference in power-loss coefficients (quantitative values are not presented for conciseness). Indeed, this result is supported by two considerations: i) the major part of $\overline{C_{PL}}$ at low rotation rates (low C_N) is derived from the mean pressure drag, in particular, that from the main body, which was not strongly affected by the angle of attack of the incoming flow (but rather by pressure difference fore and aft the body) and ii) as ζ increased, from previous results

(Assi et al., 2019; Carvalho et al., 2021; Carvalho and Assi, 2023a) it is known that $\overline{C_D}$ becomes less relevant compared with the power required to spin the rods against viscous traction, i.e., $\overline{C_N}$. Neither of these two considerations depend on the angle of the incoming flow, thus they justify that in terms of power consumption, α did not impart significant changes to $\overline{C_{PL}}$, $\overline{C_N}$ or $\overline{C_D}$.

4. Conclusion

We have investigated whether a system – comprised of eight peripheral rotating rods (45° apart) fitted around a main cylinder – behaved omnidirectionally. An incoming uniform flow at different angles of attack α was imposed. The control mechanism operated with progressively larger levels of actuation ζ . Our comparison involved two angular speed configurations $\omega_n = \omega_n(\zeta)$, constrained to the same input kinetic energy: One in which all rods spun with the same angular velocity (case 0), and another, where their velocities were inspired by the potential-flow field around a bare cylinder (case 1).

Wake topology visualisation through vorticity contours rendered evident that both systems eliminated vortex shedding and reduced wake width provided either of the following conditions was met: 1) appropriate configurations of α together with sufficiently high ω_n) or 2) to increase ω_n indefinitely.

As the rods spun faster, they injected momentum into the boundary layer and delayed separation, promoting a smaller region of low pressure aft the system, independently of α ; thus reducing mean drag. Also, for both cases, the presence of the rods led to mean drag upon the main body lower than that of a plain cylinder under any value of ζ . Our investigation of the power consumption, based on the work of Shukla and Arakeri (2013), demonstrated that the power loss coefficient did not to depend on α . The analysis of the hydrodynamic loads upon the rods showed that their inversion upon specific rods was fundamental to mitigate mean drag and mean lift.

Aside from these similarities, the two systems produced completely different mean lift. In case 0, the system presented strong directionality and failed to mitigate lift, especially at large α . In fact, for this system, lift increased monotonically with α . Asymmetrical distribution of positive and negative vorticity contours in the downstream flow highlighted the imbalance that led to the net lift upon the entire system. Our analysis revealed, in particular, that this force stemmed from the rods' contributions.

In case 1, the system showed an omnidirectional property: Regardless of the angle of attack, case 1 was capable of reducing mean drag and eliminating mean lift. In contrast to case 0, vorticity contours exhibited symmetry between negative and positive-oriented regions with equal number of contours. Consequently, RMS of lift of case 1 was one order of magnitude lower than in case 0 and vanished more quickly. Furthermore, curves $\overline{C_L} \times \alpha$ followed a tendency of flattening with ζ . Thus, case 1 configuration behaved ever "more omnidirectionally" with faster angular speeds. We have also discerned that the lift of case 0 was not eliminated by feeding the entire system with more actuating power. Rather, it is essential to weight different rods with different velocities in order to achieve this goal.

In practical terms, perhaps anticipating a possible technological application, the present investigation showed that a bluff body surrounded by 8 rotating rods based on a speed-control approach inspired by the potential-flow velocity field proved to be good enough to achieve omnidirectional flow control. Future research should concentrate on the optimisation of angular velocities ω_n targeting minimal power consumption, drag reduction or even generation of a useful lift force and expand this analysis to turbulent regime.

Acknowledgments

IAC is grateful to CAPES Brazilian Ministry of Education for his PhD scholarship and to the National Laboratory for Scientific Computing (LNCC/MCTI, Brazil) for providing HPC resources of the SDumont supercomputer. GRSA acknowledges the support of FAPESP, Brazil (2011/00205-6) and CNPq, Brazil (306146/2019-3). We gratefully acknowledge the support of the RCGI Research Centre for Greenhouse Gas Innovation, hosted by the University of São Paulo, Brazil and sponsored by FAPESP (2020/15230-5) and Shell Brasil.

References

- Assi, G.R., Bearman, P., Kitney, N., 2009. Low drag solutions for suppressing vortex-induced vibration of circular cylinders. Journal of Fluids and Structures 25, 666–675.
- Assi, G.R.S., Orselli, R.M., Silva-Ortega, M., 2018. Suppression of vortex shedding with rotating wake-control cylinders: Numerical investigation at a moderate reynolds number, in: International Conference on Offshore Mechanics and Arctic Engineering, American Society of Mechanical Engineers. p. V002T08A060.
- Assi, G.R.S., Orselli, R.M., Silva-Ortega, M., 2019. Control of vortex shedding from a circular cylinder surrounded by eight rotating wake-control cylinders at Re= 100. Journal of Fluids and Structures 89, 13–24.

- Baek, H., Karniadakis, G.E., 2009. Suppressing vortex-induced vibrations via passive means. Journal of Fluids and Structures 25, 848–866.
- Bearman, P., 1967. The effect of base bleed on the flow behind a two-dimensional model with a blunt trailing edge.

 Aeronautical Quarterly 18, 207–224.
- Blackburn, H.M., Henderson, R.D., 1999. A study of two-dimensional flow past an oscillating cylinder. Journal of Fluid Mechanics 385, 255–286.
- Blevins, R.D., 1990. Flow-induced vibration. 2 ed., Van Nostrand Reinhold, New York.
- Carvalho, I.A., 2023. Enhanced control of bluff-body wakes by the interference of rotating rods. Ph.D. thesis. Department of Mechanical Engineering, University of São Paulo.
- Carvalho, I.A., Assi, G.R.S., 2022. Enhanced control of the turbulent flow past a circular cylinder with rotating rods inspired by an inviscid solution. Journal of Fluids and Structures 113, 103652. URL: https://www.sciencedirect.com/science/article/pii/S0889974622000913, doi:https://doi.org/10.1016/j.jfluidstructs.2022.103652.
- Carvalho, I.A., Assi, G.R.S., 2023a. Active control of vortex shedding past finite cylinders under the effect of a free surface. Physics of Fluids 35, 045130. URL: https://doi.org/10.1063/5.0147760, doi:10.1063/5.0147760, arXiv:https://pubs.aip.org/aip/pof/article-pdf/doi/10.1063/5.0147760/16831213/045130_1_5.0147760.pdf. 045130.
- Carvalho, I.A., Assi, G.R.S., 2023b. Passive control of vortex-shedding past finite cylinders under the effect of a free surface. Physics of Fluids 35. URL: https://doi.org/10.1063/5.0134730, doi:10.1063/5.0134730, arXiv:https://pubs.aip.org/aip/pof/article-pdf/doi/10.1063/5.0134730/16778152/015109_1_online.pdf. 015109.
- Carvalho, I.A., Assi, G.R.S., Orselli, R.M., 2021. Wake control of a circular cylinder with rotating rods: Numerical simulations for inviscid and viscous flows. Journal of Fluids and Structures 106, 103385. URL: https://www.sciencedirect.com/science/article/pii/S0889974621001687, doi:https://doi.org/10.1016/j.jfluidstructs.2021.103385.
- Chen, W.L., Xin, D.B., Xu, F., Li, H., Ou, J.P., Hu, H., 2013. Suppression of vortex-induced vibration of a circular cylinder using suction-based flow control. Journal of Fluids and Structures 42, 25–39.
- Choi, H., Jeon, W.P., Kim, J., 2008. Control of flow over a bluff body. Annu. Rev. Fluid Mech. 40, 113-139.
- Cicolin, M.M., Buxton, O.R.H., Assi, G.R.S., Bearman, P.W., 2021. The role of separation on the forces acting on a circular cylinder with a control rod. Journal of Fluid Mechanics 915.
- Dolci, D.I., Carmo, B.S., 2019. Bifurcation analysis of the primary instability in the flow around a flexibly mounted circular cylinder. Journal of Fluid Mechanics 880, R5.
- Du, L., Sun, X., 2015. Suppression of vortex-induced vibration using the rotary oscillation of a cylinder. Physics of Fluids 27.
- Fujarra, A.L.C., Rosetti, G.F., de Wilde, J., Gonçalves, R.T., 2012. State-of-art on vortex-induced motion: A comprehensive survey after more than one decade of experimental investigation, in: Proceedings of the OMAE International Conference on Offshore Mechanics and Arctic Engineering, pp. 561–582.
- Gerrard, J.H., 1966. The mechanics of the formation region of vortices behind bluff bodies. Journal of fluid mechanics

- 25, 401-413.
- Korkischko, I., Meneghini, J., 2012. Suppression of vortex-induced vibration using moving surface boundary-layer control. Journal of Fluids and Structures 34, 259–270.
- Korkischko, I., Meneghini, J.R., 2011. Volumetric reconstruction of the mean flow around circular cylinders fitted with strakes. Experiments in fluids 51, 1109–1122.
- Marquet, O., Sipp, D., Jacquin, L., 2008. Sensitivity analysis and passive control of cylinder flow. Journal of Fluid Mechanics 615, 221–252.
- Mittal, S., 2001. Control of flow past bluff bodies using rotating control cylinders. Journal of fluids and structures 15, 291–326.
- Mittal, S., Kumar, B., 2003. Flow past a rotating cylinder. Journal of fluid mechanics 476, 303-334.
- Mittal, S., Raghuvanshi, A., 2001. Control of vortex shedding behind circular cylinder for flows at low Reynolds numbers. International Journal for Numerical Methods in Fluids 35, 421–447.
- Modi, V., Fernando, M.S.U.K., Yokomizo, T., 1990. Drag reduction of bluff bodies through moving surface boundary layercontrol, in: 28th Aerospace Sciences Meeting, p. 298.
- Moukalled, F., Mangani, L., Darwish, M., Moukalled, F., Mangani, L., Darwish, M., 2016. The finite volume method. Springer.
- Norberg, C., 2001. Flow around a circular cylinder: aspects of fluctuating lift. Journal of fluids and structures 15, 459–469.
- Patankar, S.V., 1980. Numerical heat transfer and fluid flow.
- Patino, G.A., Gioria, R.S., Meneghini, J.R., 2017. Evaluating the control of a cylinder wake by the method of sensitivity analysis. Physics of Fluids 29, 044103. doi:10.1063/1.4979482, arXiv:https://doi.org/10.1063/1.4979482.
- Shukla, R.K., Arakeri, J.H., 2013. Minimum power consumption for drag reduction on a circular cylinder by tangential surface motion. Journal of Fluid Mechanics 715, 597–641. doi:10.1017/jfm.2012.537.
- Silva-Ortega, M., Assi, G.R.S., 2017a. Flow-induced vibration of a circular cylinder surrounded by two, four and eight wake-control cylinders. Experimental Thermal and Fluid Science 85, 354–362.
- Silva-Ortega, M., Assi, G.R.S., 2017b. Suppression of the vortex-induced vibration of a circular cylinder surrounded by eight rotating wake-control cylinders. Journal of Fluids and Structures 74, 401–412.
- Silva-Ortega, M., Assi, G.R.S., Cicolin, M.M., 2015. Hydrodynamic Force Measurements on a Circular Cylinder Fitted With Peripheral Control Cylinders: Preliminary Results on the Development of VIV Suppressors, in: International Conference on Offshore Mechanics and Arctic Engineering, American Society of Mechanical Engineers. p. V002T08A062.
- Strykowski, P.J., Sreenivasan, K.R., 1990. On the formation and suppression of vortex shedding at low reynolds numbers. Journal of Fluid Mechanics 218, 71–107.
- Vakil, A., Green, S.I., 2009. Drag and lift coefficients of inclined finite circular cylinders at moderate reynolds numbers. Computers & Fluids 38, 1771–1781.
- Von Kármán, T., 1954. Aerodynamics: selected topics in the light of their historical development. Cornell University Press.
- Williamson, C.H.K., Govardhan, R., 2004. Vortex-induced vibrations. Annu. Rev. Fluid Mech. 36, 413-455.

Wu, W., Wang, J., Jiang, S., Xu, L., Sheng, L., 2016. Flow and flow control modeling for a drilling riser system with auxiliary lines. Ocean Engineering 123, 204–222.

Zdravkovich, M.M., 1981. Review and classification of various aerodynamic and hydrodynamic means for suppressing vortex shedding. Journal of Wind Engineering and Industrial Aerodynamics 7, 145–189.